Acta Mech
https://doi.org/10.1007/s00707-019-02409-8

ORIGINAL PAPER

Emanuele Grossi · Ahmed A. Shabana

Analysis of high-frequency ANCF modes: Navier–Stokes physical damping and implicit numerical integration

Received: 21 September 2018 / Revised: 26 January 2019

Abstract This paper is concerned with the study of the high-frequency modes resulting from the use of the finite element *absolute nodal coordinate formulation* (ANCF) in multibody system (MBS) applications. The coupling between the cross-sectional deformations and bending and extension of ANCF beam and plate elements produces high-frequency modes which negatively impact the computational efficiency. In this paper, two new and fundamentally different approaches are proposed to efficiently solve stiff systems of differential/algebraic equations by filtering and/or damping out ANCF high-frequency modes. A new objective large rotation and large deformation *viscoelastic constitutive model* defined by the Navier–Stokes equations, widely used for fluids, is proposed for ANCF solids. The proposed Navier–Stokes viscoelastic constitutive model is formulated in terms of a diagonal damping matrix, allows damping out insignificant high-frequency modes, and leads to zero energy dissipation in the case of rigid body motion. The second approach, however, is numerical and is based on enhancing the *two-loop implicit sparse matrix numerical integration* (TLISMNI) method by introducing a new stiffness detection error control criterion. The new criterion avoids unnecessary reductions in the time step and minimizes the number of TLISMNI outer loop iterations required to achieve convergence. The TLISMNI method ensures that the MBS algebraic constraint equations are satisfied at the position, velocity, and acceleration levels, efficiently exploits sparse matrix techniques, and avoids numerical force differentiation. The performance of the TLISMNI/Adams algorithm using the proposed error criterion is evaluated by comparison with the TLISMNI/HHT method and the explicit predictor–corrector, variable-order, and variable step-size Adams methods. Several numerical examples are used to evaluate the accuracy, efficiency, and damping characteristics of the new nonlinear viscoelastic constitutive model and the TLISMNI procedure.

1 Introduction

ANCF elements, based on accurate geometric representation, can capture deformation modes that cannot be captured using conventional structural elements such as beams, plates, and shells. Use of the continuum mechanics approach with ANCF elements allows for capturing the coupling between the cross-sectional deformation and the beam centerline or plate mid-surface displacements, thus relaxing the assumptions of Euler–Bernoulli and Timoshenko beam theories [4,39]. Nonetheless, some ANCF coupled deformation high-frequency modes adversely affect the computational efficiency and can be source of numerical problems, despite having a negligible effect on the solution accuracy.

E. Grossi · A. A. Shabana (✉)
Department of Mechanical and Industrial Engineering, University of Illinois at Chicago, Chicago, IL 60607, USA
E-mail: shabana@uic.edu

E. Grossi
E-mail: egross20@uic.edu

There are two fundamentally different approaches that are commonly used to handle ANCF high-frequency modes. The first approach employs physical internal damping, while the second approach is based on using implicit numerical integration methods, some of which are based on controllable numerical dissipation, referred to as *numerical damping*. With regard to the first approach, viscoelastic constitutive models can be used with confidence to damp out high-frequency oscillations as long as they reflect the physical behavior of the system without violating mechanics principles. Accurate energy description is also necessary to perform reliable durability and noise, vibration, and harshness (NVH) analyses. With regard to the numerical integration approach, numerical damping must be used with care because the effect of high-frequency modes cannot be arbitrarily filtered out in all applications. The *two-loop implicit sparse matrix numerical integration* (TLISMNI) method was proposed to address the limitations of existing low-order implicit integration methods which can filter out contributions of important modes [29]. Another important problem which can undermine the efficiency and convergence rate of ANCF elements is the locking phenomenon, which can be solved by selecting proper locking alleviation techniques [14]. The specific contributions of this paper are summarized as follows:

(i) A new objective viscoelastic constitutive model which accounts for both material and geometric nonlinearities, does not damp out rigid body motion, and allows for filtering out high-frequency modes in the case of small and large deformations is proposed. The elastic response is described using general hyperelastic material laws which can accurately capture the elastic deformation of flexible and incompressible materials. The viscous damping model, on the other hand, is based on a generalization of the Navier–Stokes constitutive equations, widely used for fluids, for the use with ANCF solids.
(ii) The relationship between the proposed Navier–Stokes viscoelastic model and existing constitutive laws is discussed in both small and large deformation scenarios. The newly implemented viscoelastic constitutive model is validated and tested in order to demonstrate that the proposed constitutive model can be used to efficiently damp out ANCF high-frequency modes and achieve CPU time saving of at least 50% when compared with the perfect elastic case.
(iii) General stiffness detection and error control criteria are developed within the TLISMNI framework to identify, during the integration process, the high-frequency and stiff components of the solution vector. The development of a robust stiffness detection scheme is important to evaluate the significance of each signal and filter out the effect of selected insignificant high-frequency oscillations. Using the stiffness detection criterion, new TLISMNI error estimation and control methods are proposed to allow avoiding unnecessary reduction in the time step size and minimizing the number of the TLISMNI outer loop iterations required to achieve convergence.
(iv) Several constrained dynamical systems are used to study the accuracy, robustness, and damping characteristics of the TLISMNI/Adams algorithm as compared to the TLISMNI/HHT and the explicit predictor–corrector Adams methods. The damping characteristics of the TLISMNI/Adams method used with the newly proposed Navier–Stokes viscoelastic constitutive model are compared with those of the TLISMNI/HHT method.

This paper is organized as follows. In Sect. 2, several existing viscoelastic constitutive models are reviewed, and the newly proposed Navier–Stokes viscoelastic constitutive model is introduced. In Sect. 3, experimental and analytical methods which can be used in the identification of the dynamic viscosity coefficients of different materials are presented. The ANCF equations of motion and generalized viscoelastic forces are introduced in Sects. 4 and 5, respectively. Sections 6 and 7 describe the TLISMNI method, and the stiffness detection and error control criteria, respectively. Section 8 presents several numerical examples used to assess the efficiency and applicability of the proposed viscoelastic constitutive model and the TLISMNI error criterion. Section 9 provides a summary and the main conclusions drawn from this study.

2 Viscoelasticity formulations

In this Section, a review of existing viscoelastic constitutive models is presented, and the Navier–Stokes viscoelastic formulation, used in this investigation for ANCF solids, is introduced.

2.1 Existing viscoelastic constitutive models

Accurate description of material behavior is necessary for developing realistic virtual prototyping models that can be used for design and analysis of automotive, heavy machinery, and aerospace systems. Most materials

dissipate energy as they deform because of internal damping, associated with physical micro- and macroscopic-level mechanisms [23]. The introduction of a physics-based internal damping is also important in order to achieve dynamic simulation efficiency by damping out high-frequency oscillations that require a small time step during the numerical integration of the equations of motion. Several linear and nonlinear viscoelastic constitutive models that can be implemented in incremental solution procedures based on the corotational FE approach can be found in the literature [5,11,32,42]. However, these models are not suited for implementation in general-purpose flexible MBS computer algorithms that are based on non-incremental solution procedures. Takahashi et al. [38] proposed using the proportional Rayleigh damping in the ANCF nonlinear equations of motion. This approach is limited to the analysis of small deformations within individual ANCF elements and leads to damping the rigid body motion. Yoo et al. [43] used the damping procedure proposed by Takahashi et al. [38] to study the oscillations of a cantilever beam with attached endpoint mass and validated the numerical results against experimental measurements. Garcia and Vallejo et al. [13] developed an objective internal damping formulation based on the linear Kelvin–Voigt constitutive model which accounts for the deviatoric and hydrostatic material response. This model, referred to in this paper as the *small strain viscoelastic model*, is not suitable for the analysis of very flexible and incompressible materials because it is based on linear constitutive equations. As reported in the literature, the use of nonlinear elastic constitutive models for large deformation problems can improve the computational efficiency of ANCF models and contributes to avoiding singular-deformation configurations that may result from using the linear elastic models [20]. Moreover, the damping matrix obtained in case of the small strain viscoelastic model leads to viscous coupling between the strain rate components and does not allow damping out high-frequency modes independently. Zhang et al. [45] proposed a viscoelastic fractional derivative ANCF model and obtained good results in several numerical examples including pendulum and cantilever beam problems. However, this approach was proposed only for two-dimensional analysis under the assumption of plane stress. Furthermore, the use of fractional derivatives requires large storage and can lead to a significant computational cost increase [26]. An objective nonlinear viscoelastic constitutive model that can be implemented in non-incremental FE formulations was proposed [22]. In this model, referred to in this paper as the *ANCF deformation gradient rate viscoelastic* (DGRV) model, the damping force vector is defined as a function of the time rate of the deformation gradients, which are determined using the **QR** decomposition of the matrix of position vector gradients. As a result, the viscous stresses not only are functions of the strain rates but also depend nonlinearly on the Green–Lagrange strain components. Further research is required to analyze the performance of the DGRV model as compared to viscoelastic formulations based on a different decomposition of the matrix of position vector gradients such as the polar decomposition theorem and using different reference coordinate systems such as the cross section or Frenet frame.

2.2 Navier–Stokes viscoelastic model

In order to capture the physical behavior of metal- and rubberlike materials in large deformation and large rotation problems, a general viscoelastic constitutive model must properly account for geometric and material nonlinearities. In the viscoelastic formulation proposed in this investigation, the nonlinear elastic behavior of very flexible and incompressible materials is captured by properly defining the strain energy density function. The material dissipation is accounted for by introducing a viscous stress defined using the incompressible Navier–Stokes equations.

The one-dimensional Kelvin–Voigt viscoelastic constitutive model is among the simplest models used in linear viscoelasticity. The total stress is defined as the sum of elastic and viscous components which result from a configuration of springs and dashpots arranged in parallel [33]. Under the assumption of infinitesimal strain, the Kelvin–Voigt constitutive model can be written in the three-dimensional case as $\boldsymbol{\sigma} = \mathbf{E} : \boldsymbol{\varepsilon}_i + \mathbf{D}_t : \dot{\boldsymbol{\varepsilon}}_i$, where $\boldsymbol{\sigma}$ is the stress tensor, $\boldsymbol{\varepsilon}_i = 1/2\left(\mathbf{J}_d + \mathbf{J}_d^T\right)$ is the infinitesimal strain tensor, $\mathbf{J}_d$ is the matrix of displacement vector gradients, and $\mathbf{E}$ and $\mathbf{D}_t$ are the fourth-order tensors of elastic and damping coefficients, respectively [5,28]. This formulation can be used to obtain the small strain viscoelastic model by introducing appropriate stress and strain measures and ensuring that the constitutive equation is frame-indifferent as

$$\boldsymbol{\sigma}_{P2} = \mathbf{E} : \boldsymbol{\varepsilon} + \mathbf{D}_t : \dot{\boldsymbol{\varepsilon}} \tag{1}$$

where $\boldsymbol{\sigma}_{P2}$ is the second Piola–Kirchhoff stress tensor, $\boldsymbol{\varepsilon} = (1/2)\left(\mathbf{J}^T\mathbf{J} - \mathbf{I}\right)$ is the Green–Lagrange strain tensor, $\mathbf{J}$ is the matrix of position vector gradients, $\mathbf{I}$ is the 3×3 identity matrix, and $\dot{\boldsymbol{\varepsilon}}$ is the time derivative of $\boldsymbol{\varepsilon}$ ([5,13]). The Kelvin–Voigt constitutive model can be generalized in a straightforward manner to the case of

nonlinear elasticity by writing the elastic component of the second Piola–Kirchhoff stress tensor as function of the strain energy density function Ψ as

$$\boldsymbol{\sigma}_{P2} = \boldsymbol{\sigma}^{e}_{P2} + \boldsymbol{\sigma}^{v}_{P2} = \frac{\partial \Psi}{\partial \boldsymbol{\varepsilon}} + \mathbf{D}_t : \dot{\boldsymbol{\varepsilon}}. \tag{2}$$

In the case of finite strain elasticity, the energy density function Ψ can be written as $\Psi = \overline{\Psi} + \Psi^{\circ}$, where Ψ° and $\overline{\Psi}$ are the volume preserving (deviatoric) and volumetric components of the energy density function, respectively. The viscous component of the stress tensor $\boldsymbol{\sigma}^{v}_{P2}$ can be conveniently written in the current configuration as

$$\boldsymbol{\sigma}^{v} = -p\mathbf{I} + \mathbf{A} : \mathbf{D} \tag{3}$$

where p is the hydrostatic pressure, $\boldsymbol{\sigma}^{v}$ is the Cauchy stress tensor, $\mathbf{I}$ is the 3×3 identity matrix, $\mathbf{A}$ is the fourth-order tensor of viscosity coefficients, and $\mathbf{D} = \left(\mathbf{J}^{-1}\right)^{T} \dot{\boldsymbol{\varepsilon}}\ \mathbf{J}^{-1}$ is the rate of deformation tensor. Under the assumption of isotropic viscous response, the viscous stress tensor can be written as a function of two independent parameters as

$$\boldsymbol{\sigma}^{v} = \left[-p + \lambda \mathrm{tr}(\mathbf{D})\right] \mathbf{I} + 2\mu \mathbf{D} \tag{4}$$

where μ is the coefficient of dynamic viscosity and $(\lambda + 2\mu/3)$ is the coefficient of bulk viscosity [12,35, 40]. For many viscoelastic materials, such as polymers, the dilatational deformation is much stiffer than the deviatoric response, and the incompressibility assumption is acceptable [32]. Motivated by these observations, the incompressibility assumption $\dot{J} = J\,\mathrm{tr}\,(\mathbf{D}) = 0$ is imposed, and in this case, Eq. (4) reduces to

$$\boldsymbol{\sigma}^{v} = -p\mathbf{I} + 2\mu \mathbf{D} \tag{5}$$

which is the Navier–Stokes constitutive equation widely used for incompressible Newtonian viscous fluids. The incompressibility condition can be enforced using a penalty method by defining the volumetric strain energy function as $\overline{\Psi} = (1/2)\, k\, (J-1)^2$, where k is a penalty coefficient. The viscous damping stress can be written in Voigt form as $\{\boldsymbol{\sigma}^{v}\} = \mathbf{D}_m\{\mathbf{D}\}$, where $\{\boldsymbol{\sigma}^{v}\} = \left[\sigma^{v}_{11}\ \ \sigma^{v}_{22}\ \ \sigma^{v}_{33}\ \ \sigma^{v}_{12}\ \ \sigma^{v}_{13}\ \ \sigma^{v}_{23}\right]^{T}$, $\{\mathbf{D}\} = [D_{11}\ \ D_{22}\ \ D_{33}\ \ D_{12}\ \ D_{13}\ \ D_{23}]^{T}$, and $\mathbf{D}_m$ is the damping matrix, defined as

$$\mathbf{D}_m = 2\mu \mathbf{I} \tag{6}$$

where $\mathbf{I}$ is the 6×6 identity matrix.

2.3 Comparison with existing viscoelastic models

In this Section, the Navier–Stokes viscoelastic model is compared with the small strain and the ANCF DGRV constitutive models. It is clear that the diagonal form of the damping matrix $\mathbf{D}_m$ defined by Eq. (6) does not couple the components of the rate of deformation tensor unlike the small strain viscoelastic model. In the latter formulation, the damping matrix leads to viscous coupling between the normal strain rates and can be written for isotropic materials as

$$\mathbf{D}_s = \begin{bmatrix} \xi + 2\beta & \xi & \xi & \\ \xi & \xi + 2\beta & \xi & \mathbf{0} \\ \xi & \xi & \xi + 2\beta & \\ & \mathbf{0} & & 2\beta\,\mathbf{I} \end{bmatrix} \tag{7}$$

where $\mathbf{I}$ and $\mathbf{0}$ in this equation are the 3×3 identity and null matrices, respectively, $\xi = (E\gamma_{v1} - 2G\gamma_{v1}\,(1-2\nu))\,/3\,(1-2\nu)$, $\beta = G\gamma_{v2}$, E and G are the elastic and shear moduli, respectively, υ is Poisson's ratio, and γ_{v1} and γ_{v2} are the dilatational and deviatoric dissipation factors, respectively. In Sect. 3.2, it is shown analytically that in the case of small deformations the coefficient of dynamic viscosity μ used in the Navier–Stokes constitutive model proposed in this investigation for ANCF solids is equivalent to β. Another advantage of the viscous Navier–Stokes damping formulation, shared with the ANCF DGRV model, is that the

matrix of damping coefficients can be written more generally as function of two different dynamic viscosity coefficients, while preserving its diagonal form as

$$\mathbf{D}_m = \begin{bmatrix} (\lambda + 2\mu)\,\mathbf{I} & \mathbf{0} \\ \mathbf{0} & 2\mu\mathbf{I} \end{bmatrix} \tag{8}$$

where λ can be identified experimentally. This form of the damping matrix ensures isotropy, neglects the Poisson damping effects, and allows independently damping out dilatational and deviatoric vibration modes. The viscous Cauchy stress tensor defined in Eq. (5) can be transformed to the reference configuration by applying the pullback operation $\boldsymbol{\sigma}^{v}_{P2} = J\,(\mathbf{J})^{-1}\,\boldsymbol{\sigma}^{v}\left[(\mathbf{J})^{-1}\right]^{T}$, and the viscoelastic constitutive model of Eq. (2) can be written as

$$\boldsymbol{\sigma}_{P2} = \frac{\partial \Psi}{\partial \boldsymbol{\varepsilon}} + 2\mu J\,(\mathbf{J})^{-1}\,\mathbf{D}\left[(\mathbf{J})^{-1}\right]^{T}. \tag{9}$$

This second Piola–Kirchhoff stress tensor is defined in the reference configuration and can be used with both the Green–Lagrange strain tensor to define the elastic forces and the tensor $(\mathbf{J})^{-1}\,\mathbf{D}\left[(\mathbf{J})^{-1}\right]^{T}$ required for the calculation of the viscous forces.

2.4 Objectivity

Structural damping forces are the result of the relative motion between the material particles. If the body experiences a pure rigid body motion, no internal friction between its particles is developed, and consequently, no damping forces are generated. It can be demonstrated analytically that the Navier–Stokes formulation leads to zero damping forces in case of rigid body motion. The Green–Lagrange deformation tensor $\boldsymbol{\varepsilon}$ is used as a measure of the deformation because it vanishes in the case of rigid body motion. The rate of deformation tensor $\mathbf{D}$ is related to the rate of change in the Green–Lagrange deformation tensor $\dot{\boldsymbol{\varepsilon}}$ by the push-forward operation $\mathbf{D} = \left(\mathbf{J}^{-1}\right)^{T}\,\dot{\boldsymbol{\varepsilon}}\,\mathbf{J}^{-1}$. In the case of rigid body motion, $\boldsymbol{\varepsilon}$ is constant, and consequently, the strain rate $\dot{\boldsymbol{\varepsilon}} = \mathbf{0}$, leading to $\mathbf{D} = \mathbf{0}$. Since the viscous damping stress depends linearly on the rate of deformation tensor, the damping forces are also zero in the case of rigid body motion.

3 Determination of the damping coefficient

The Navier–Stokes equations are used mainly to describe the viscosity of fluids and are not widely used for describing the damping of solids. In order to be able to use these equations for solids modeled using ANCF elements, it is necessary to define the viscosity coefficients that appear in these equations. While this paper is not focused on the experimental identification of the viscosity coefficients, in this Section an overview of some popular experimental procedures used to determine the coefficients of dynamic viscosity of rubberlike and steel materials is presented. These experimentally determined coefficients can be used in the Navier–Stokes viscoelastic constitutive model proposed in this investigation for ANCF solids. In the case of small deformations, the analytical relationship between the coefficient of dynamic viscosity μ and the deviatoric dissipation factor γ_{v2}, often used in the literature, is defined.

3.1 Experimental testing

The coefficient of dynamic viscosity μ is an important measure of the internal damping characteristics of materials. Several experimental methods have been developed to identify the viscosity of metals, polymers, rubbers, and composite materials in the solid state. Among the most popular techniques for measuring high viscosities ($\mu > 10^8$ Pa $\cdot$ s) are the *beam bending*, *bar torsion,* and *penetration methods*, while for low viscosities ($\mu < 10^8$ Pa $\cdot$ s), the *rotational viscometer* methods are preferred [9,19,36,37]. Kobayashi et al. [18] designed an apparatus which accurately measures the Newtonian viscosity of solids up to 10^{14} Pa $\cdot$ s. A constant shear load is applied to a cubic test specimen, and the viscoelastic deformation is measured using a laser interferometer. The load/displacement relation is converted into a stress/strain relation, and the viscosity coefficient is defined as $\mu = \sigma^{s}/(\mathrm{d}\varepsilon^{s}/\mathrm{d}t)$, where σ^{s} and ε^{s} are the shear stress and strain, respectively.

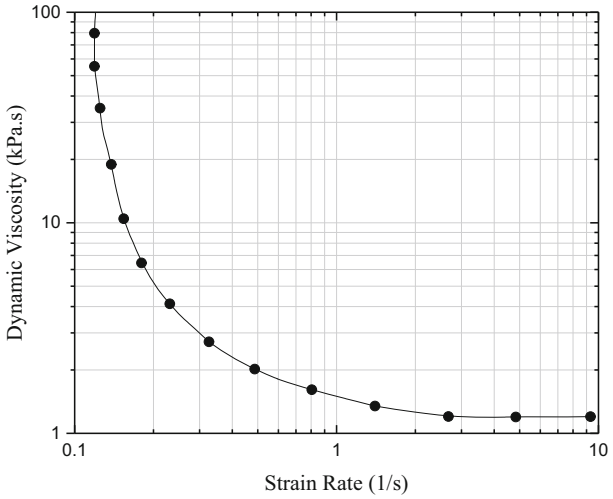

Fig. 1 Dynamic viscosity of low-carbon steel in logarithmic scale [27]

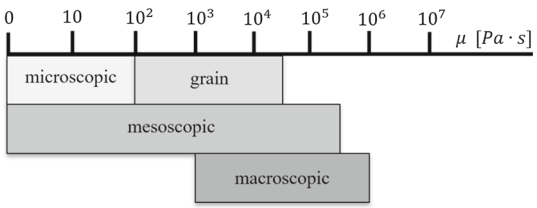

Fig. 2 Dynamic viscosity of steels at different structural levels [25]

Several studies have been performed to identify the shear viscosity of rubber and materials that have rubber contents. It was found that for most rubberlike materials the value of the dynamic viscosity ranges between 1 and 10^3 Pa · s in the shear rate range $1 - 10^2$ 1/s [2,6,41]. A popular experiment used to calculate the viscosity of metals is the *compressed cylindrical shell*, in which a hollow metal cylinder is deformed axisymmetrically by applying a varying internal pressure. Using this method, Serikov [27] computed the value of dynamic viscosity of low-carbon steel and Z3CN18-10 steel as a function of the strain rate (Fig. 1). In 2002, Savenkov and Meshcheryakov [25] applied the method of pulse loading of specimens to calculate the coefficient of dynamic viscosity of different steels and showed that, at the macroscopic level, μ ranges from 10^3 to 10^6 Pa · s (Fig. 2).

3.2 Dynamic viscosity coefficient and dissipation factor

Using the principles of vibration theory and under the assumption of small deformations, it is possible to identify the relationship between the coefficient of dynamic viscosity μ and the dissipation factor γ_{v2} used in the small strain viscoelastic model. The generalized standard model of a linear viscoelastic material can be expressed in the time domain using a linear ordinary differential equation of arbitrary order [23] as follows:

$$\sigma + \sum_{n=1}^{\infty} z_n \frac{d^n \sigma}{\mathrm{d}t^n} = E\varepsilon + \sum_{n=1}^{\infty} u_n \frac{d^n \varepsilon}{\mathrm{d}t^n} \tag{10}$$

where n is the order of the differential equation, σ is the stress, ε is the strain, and z and u are constants. In the case of sinusoidal stress and strain of the form $\sigma = \sigma_0 e^{j\omega t}$ and $\varepsilon = \varepsilon_0 e^{j\omega t}$, respectively, where ω is the excitation frequency, σ_0 and ε_0 are the initial stress and strain, respectively, Eq. (10) can be written in the frequency domain as $\sigma_0/\varepsilon_0 = [c_1(\omega) + jc_2(\omega)]/[d_1(\omega) + jd_2(\omega)]$, where $c_1(\omega)$, $c_2(\omega)$, $d_1(\omega)$ and $d_2(\omega)$ are functions of the frequency ω, and $j = \sqrt{-1}$. The right-hand side of the equation σ_0/ε_0 can be defined as a single complex variable G^*, leading to $\sigma_0/\varepsilon_0 = \sigma/\varepsilon = G^* = G_1 + jG_2$, where G_1 and G_2 are functions of ω. The ratio between the imaginary and real parts of G^* is commonly referred to as the *loss factor*

$\delta = G_2/G_1$, which is a measure of the energy dissipation associated with the viscoelastic damping. The loss factors of different materials have been obtained experimentally as functions of the excitation frequency and temperature [23,33]. In the case of linear viscoelastic response, it is possible to prove that $d\varepsilon/dt = j\,|\omega|\,\varepsilon$ and the stress/strain rate relationship can be written as $\sigma = G_1\varepsilon + (G_1\delta/|\omega|)\,(d\varepsilon/dt)$. If the Kelvin–Voigt viscoelastic model is used, the relation between the coefficient of dynamic viscosity μ and the loss factor δ is derived in a straightforward manner as $\mu = G_1\delta/|\omega|$. The dissipation factor γ_{v2} which appears in Eq. (7) is defined in the time domain as $\gamma_{v2} = \delta_{v2}/|\omega|$, from which it follows that $\mu = G\gamma_{v2} = \beta$, where G is the shear modulus and δ_{v2} is the shear loss factor.

4 ANCF equations of motion

The use of ANCF elements eliminates the need for using an incremental corotational solution procedure and allows for directly using the objective Navier–Stokes equations for defining the damping forces in the case of solids. This is attributed to the fact that absolute position vectors and position vector gradients are used as nodal coordinates. The Navier–Stokes equations are linear functions of the rate of the position gradients, and this facilitates the definition of the ANCF Navier–Stokes damping forces as discussed in the following Section. Furthermore, the initial geometry of an ANCF mesh can be accurately described without the need for converting a CAD B-splines or NURBS mesh to an analysis mesh. Figure 3 shows that an ANCF body can be described using straight, reference, and current configurations, whose associated volumes and position vectors (parameters) are V, V_0, v and $\mathbf{x}$, $\mathbf{X}$, $\mathbf{r}$, respectively. The global position vector of an arbitrary point on an ANCF element j can be expressed in the current and reference configurations as $\mathbf{r}^j = \mathbf{S}^j(x, y, z)\mathbf{e}^j(t)$ and $\mathbf{X}^j = \mathbf{S}^j(x, y, z)\mathbf{e}_0^j(t)$, respectively, where $\mathbf{S}^j$ is the shape function matrix expressed in terms of the element spatial coordinates x, y, and z, $\mathbf{x} = \begin{bmatrix} x & y & z \end{bmatrix}^T$, $\mathbf{e}^j$, and $\mathbf{e}_0^j$ are the element nodal coordinates in the reference and current configurations, respectively, and t is time [28]. In the case of three-dimensional fully parameterized ANCF elements, the nodal coordinate vector of element j at note k consists of absolute position and gradient coordinates and can be written as $\mathbf{e}^{jk} = \left[\left(\mathbf{r}^{jk}\right)^T \left(\partial\mathbf{r}^{jk}/\partial x\right)^T \left(\partial\mathbf{r}^{jk}/\partial y\right)^T \left(\partial\mathbf{r}^{jk}/\partial z\right)^T \right]^T$. The mapping between the element volumes in the current and reference configurations can be described in a straightforward manner using the determinant of the matrix of position vector gradients J^j as $dv^j = J^j dV_0^j$, where $\mathbf{J}^j = \partial\mathbf{r}^j/\partial\mathbf{X}^j$. If the mesh geometry is initially curved, the volume integration can be further simplified by introducing a straight reference configuration, which can be derived from the reference configuration using the relationship $dV_0^j = J_0^j dV^j$, where $\mathbf{J}_0^j = \partial\mathbf{X}^j/\partial\mathbf{x}^j$. Moreover, the straight configuration can be directly mapped to the reference configuration as $dv^j = J_e^j dV^j$, where $\mathbf{J}_e^j = \partial\mathbf{r}^j/\partial\mathbf{x}^j$ and $J_e^j = |\mathbf{J}_e^j|$. It can be shown that $\mathbf{J}^j = \partial\mathbf{r}^j/\partial\mathbf{X}^j = \left(\partial\mathbf{r}^j/\partial\mathbf{x}^j\right)\left(\partial\mathbf{x}^j/\partial\mathbf{X}^j\right) = \mathbf{J}_e^j\left(\mathbf{J}_0^j\right)^{-1}$.

Having defined the initial geometry correctly, the equations of motion of a flexible ANCF body can be derived from the principle of virtual work in dynamics, which can be written in the case of unconstrained

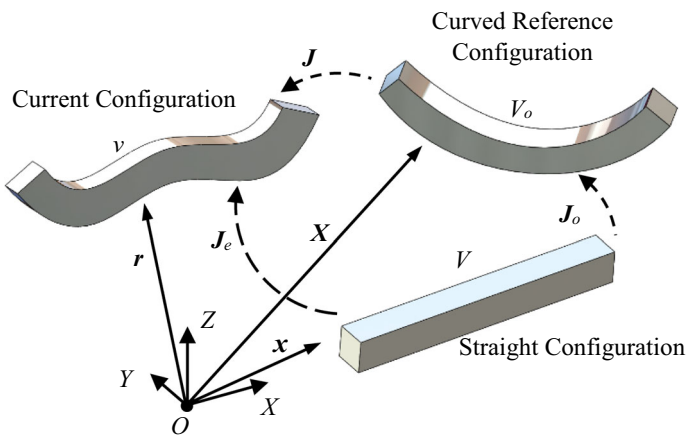

Fig. 3 Current, reference, and straight configurations

motion as $\delta W_i = \delta W_s + \delta W_{ex}$. The virtual work of the inertia forces can be written as $\delta W_i = (\mathbf{M}\ddot{\mathbf{e}})^T \delta\mathbf{e}$, where $\mathbf{M}$ is the body symmetric mass matrix, $\mathbf{e}$ is the vector of body nodal coordinates, and $\ddot{\mathbf{e}}$ is the vector of body nodal accelerations. The virtual work of the internal forces is calculated as $\delta W_s = \mathbf{Q}_s^T \delta\mathbf{e}$, where $\mathbf{Q}_s$ is the vector of generalized body internal forces, which includes elastic and internal damping forces. The virtual work of the external forces is defined as $\delta W_{ex} = \mathbf{Q}_{ex}^T \delta\mathbf{e}$, where $\mathbf{Q}_{ex}$ is the vector of generalized body external and constraint forces. By substituting the expressions for the virtual work of the inertia, internal, and external forces into the principle of virtual work, the ANCF equations of motion of the body can be written as

$$\mathbf{M}\ddot{\mathbf{e}} + \mathbf{Q}_s - \mathbf{Q}_{ex} = \mathbf{0}. \tag{11}$$

This equation can be solved for the accelerations which can be integrated numerically to determine the coordinates and velocities.

5 Generalized viscoelastic forces

The virtual work of the internal forces for an ANCF element j can be written as

$$\delta W_s^j = -\int_{V_0^j} \boldsymbol{\sigma}_{P2}^j : \delta\boldsymbol{\varepsilon}^j dV_0^j = \delta W_e^j + \delta W_d^j \tag{12}$$

where $\delta W_e^j = -\int_{V_0^j} \left(\partial\Psi/\partial\boldsymbol{\varepsilon}^j\right) : \delta\boldsymbol{\varepsilon}^j dV_0^j$ is the virtual work of the internal elastic forces, $\delta W_d^j = -\int_{V_0^j} 2\mu J^j \left(\mathbf{J}^j\right)^{-1} \mathbf{D}^j \left[\left(\mathbf{J}^j\right)^{-1}\right]^T : \delta\boldsymbol{\varepsilon}^j dV_0^j$ is the virtual work of the viscous damping forces, and $\delta\boldsymbol{\varepsilon}^j$ is the virtual change in the Green–Lagrange strain tensor. Because the rate of deformation tensor can be written as $\mathbf{D}^j = \left[\left(\mathbf{J}^j\right)^{-1}\right]^T \dot{\boldsymbol{\varepsilon}}^j \left(\mathbf{J}^j\right)^{-1}$, one can write the virtual work of the damping forces as

$$\begin{aligned}
\delta W_d^j &= -\int_{V_0^j} J^j \left(\mathbf{J}^j\right)^{-1} 2\mu \left[\left(\mathbf{J}^j\right)^{-1}\right]^T \dot{\boldsymbol{\varepsilon}}^j \left(\mathbf{J}^j\right)^{-1} \left[\left(\mathbf{J}^j\right)^{-1}\right]^T : \delta\boldsymbol{\varepsilon}^j dV_0^j \\
&= -\int_{V_0^j} 2\mu J^j \left(\mathbf{C}_r^j\right)^{-1} \dot{\boldsymbol{\varepsilon}} \left(\mathbf{C}_r^j\right)^{-1} : \delta\boldsymbol{\varepsilon}^j dV_0^j
\end{aligned} \tag{13}$$

where $\mathbf{C}_r^j = \left(\mathbf{J}^j\right)^T \mathbf{J}^j$ is the right Cauchy–Green deformation tensor. The generalized viscous damping forces associated with the ANCF nodal coordinates can be computed at any integration point using the virtual change in the strains $\delta\boldsymbol{\varepsilon}^j = \left(\partial\boldsymbol{\varepsilon}^j/\partial\mathbf{e}^j\right)\delta\mathbf{e}^j$ as

$$\left(\mathbf{Q}_d^j\right)^T = -2\mu J^j \left[\left(\mathbf{C}_r^j\right)^{-1} \dot{\boldsymbol{\varepsilon}}^j \left(\mathbf{C}_r^j\right)^{-1}\right] : \frac{\partial\boldsymbol{\varepsilon}^j}{\partial\mathbf{e}^j} \quad . \tag{14}$$

The vector of generalized elastic forces depends on the definition of the deviatoric strain energy density function Ψ°.

The linear *Hooke's law* is mainly suited for the small deformation problems, while the *neo-Hookean* and *Mooney–Rivlin* constitutive equations are suited for studying the nonlinear behavior of materials such as rubber and biological tissues. In the case of the generalized Hooke's law, the vector of elastic forces can be defined at the integration points as

$$\left(\mathbf{Q}_e^j\right)^T = \left(\frac{\partial\boldsymbol{\varepsilon}_m^j}{\partial\mathbf{e}^j}\right)^T \mathbf{A}_d \mathbf{E}_m^j \boldsymbol{\varepsilon}_m^j \tag{15}$$

where $\mathbf{E}_m^j$ is the matrix of elastic coefficients, $\boldsymbol{\varepsilon}_m^j$ is the Green–Lagrange strain tensor in Voigt form, and $\mathbf{A}_d$ is a 6×6 diagonal matrix with diagonal elements $(1,\ 1,\ 1,\ 2,\ 2,\ 2)$ [28].

In the case of incompressible neo-Hookean and Mooney–Rivlin constitutive models, the expression of the vector of elastic forces at any integration point can be defined, respectively, as

$$\left.\begin{aligned}\left(\mathbf{Q}_e^j\right)^T &= \frac{\varphi}{2}\frac{\partial\left(tr\left(\mathbf{C}^j\right)\right)}{\partial\mathbf{e}^j} + k\left(J^j-1\right)\frac{\partial J^j}{\partial\mathbf{e}^j}\\ \left(\mathbf{Q}_e^j\right)^T &= \left[\mu_{10}+\mu_{01}\left(tr\left(\mathbf{C}^j\right)\right)\right]\frac{\partial\left(tr\left(\mathbf{C}^j\right)\right)}{\partial\mathbf{e}^j} - \frac{\mu_{01}}{2}\frac{\partial\left[tr\left(\left(\mathbf{C}^j\right)^2\right)\right]}{\partial\mathbf{e}^j} + k\left(J^j-1\right)\left(\frac{\partial J^j}{\partial\mathbf{e}^j}\right)^T\end{aligned}\right\} \tag{16}$$

where φ, μ_{10}, and μ_{01} are material constants, k is the incompressibility constant, and $\mathbf{C}$ is the right Cauchy–Green deformation tensor [20]. From Eq. (12), it follows that the vector of generalized internal forces associated with the nodal coordinates of the ANCF element j can be written as $\mathbf{Q}_s^j = \mathbf{Q}_e^j + \mathbf{Q}_d^j$. The vector of body internal forces $\mathbf{Q}_s$ can be obtained using a standard FE assembly procedure as $\mathbf{Q}_s = \sum_{i=1}^{n_e}\left(\mathbf{B}^j\right)^T\mathbf{Q}_s^j$, where $\mathbf{B}^j$ is a Boolean matrix and n_e is the number of elements of the ANCF mesh.

5.1 Internal force computations

The nonlinear ANCF internal forces are evaluated using Gauss quadrature formulas. The large number of quadrature base points which is required to integrate ANCF elements can make the integration process computationally expensive, especially in the case of large meshes. For this reason, a parallel computing strategy is used in the calculation of the ANCF internal forces. A parallel computation scheme is developed using the OpenMP (Open Multi-Processing) parallel programming to allow for computing the element internal forces simultaneously using different threads, as shown in Fig. 4 [7]. The boundaries of the parallel region are defined using the commands *!$OMP parallel do* / *!$OMP end parallel do*. The variables defined in common blocks can be made private to each thread using the command *!$OMP threadprivate*. Synchronization techniques are used to avoid data conflicts which can occur when global variables are updated by each thread inside the parallel loop. In particular, a critical region is created using the commands *!$OMP critical* / *!$OMP end critical*, during the assembly process of the element internal forces.

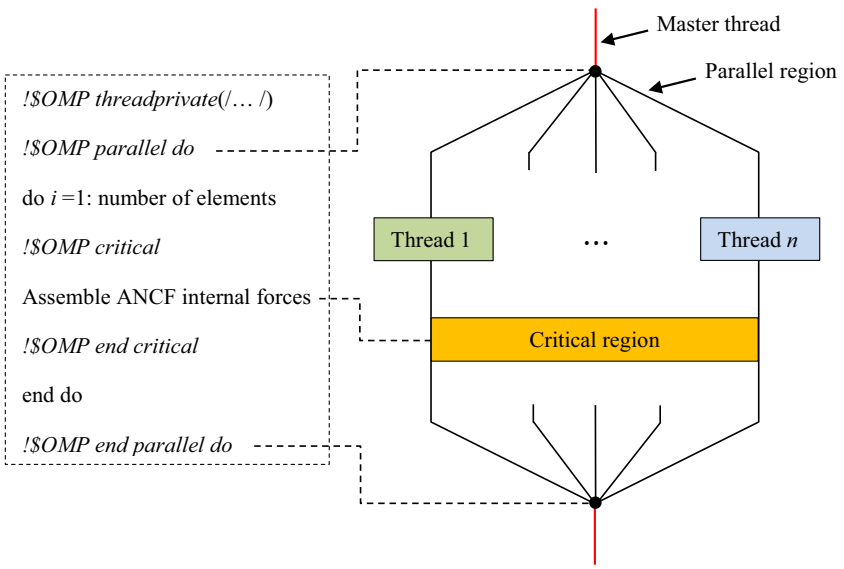

Fig. 4 Parallelization flowchart

5.2 Verification

In this Section, the proposed internal damping model is verified against analytical and numerical results using a benchmark problem [22]. Figure 5a shows a mass–viscoelastic rod system of length 0.1 m, square cross-sectional area 0.01×0.01 m^2, density 1000 kg/m^3, Poisson ratio 0.3, and Young's modulus 5×10^6 N/m^2. The flexible rod, modeled using one fully parameterized ANCF beam element, is rigidly attached to the ground at the left end and to a mass at the right end. The oscillation of the system is generated by giving the mass an initial velocity of 0.01 m/s. The volumetric and deviatoric dissipation factors are assumed equal to 0.0001 s. A mass–spring–damper system with equivalent stiffness and damping coefficients $k = 5 \times 10^3$ N/m^2 and $c = 0.5$ Ns/m^2, respectively, and known analytical solution is introduced for the sake of verification (Fig. 5b). Because the problem is in the range of small deformations, the coefficient of dynamic viscosity is calculated using the analytical relation described in Sect. 3.2 as $\mu = 192\,\text{Pa} \cdot \text{s}$. Figure 6 shows a comparison between the x-displacement of the mass using the proposed viscoelastic formulation, the ANCF DGRV model, and the mass–spring–damper system. In general, a very good agreement between the analytical and numerical results is obtained in terms of both amplitude and frequency of oscillation.

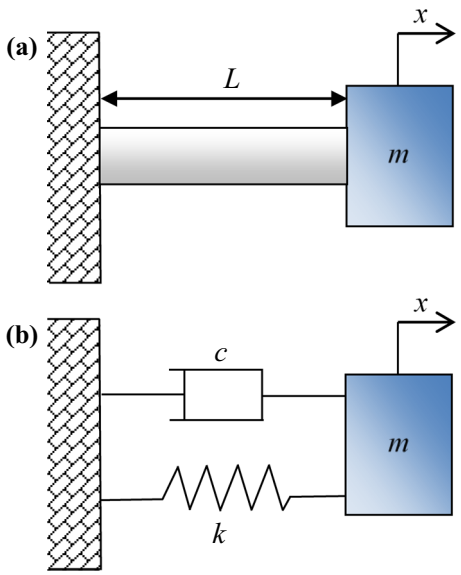

Fig. 5 **a** Mass with viscoelastic rod; **b** mass–spring–damper system

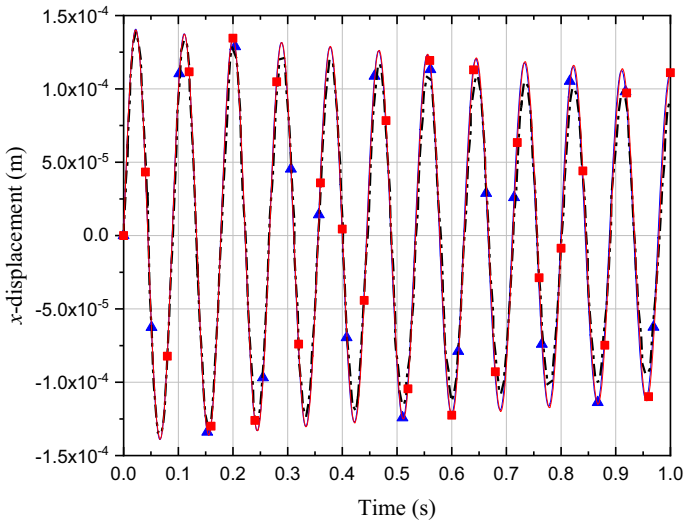

Fig. 6 x-displacement of the mass (—■— proposed model, —▲— mass–spring–damper, -·-·- ANCF DGRV model)

6 Numerical solution of ANCF equations

Introducing physical damping is not necessary only for accurate virtual prototyping, but also for improving the computational efficiency by damping out insignificant high-frequency modes. Another method which can be used to filter out ANCF high-frequency modes is to use appropriate numerical integration algorithms. In this Section, an overview of existing numerical integration methods used to solve stiff dynamical systems is provided.

6.1 Background

Explicit numerical integration methods, such as the predictor–corrector Adams method [31], are widely used in the computer solution of MBS equations. However, such explicit methods often fail or become inefficient when the equations to be solved are stiff. Some existing low-order implicit numerical integration methods which have numerical damping, such as HHT, are widely used in the solution of stiff differential equations [16]. Such methods, however, must be used with care because of the tendency of filtering out modes which can be significant. While filtering out significant high-frequency modes can be avoided by properly reducing the amount of numerical dissipation, it was shown that for systems with dominant high-frequency oscillations an excessive reduction in the amount of numerical damping can adversely impact the convergence [45]. For this reason, general-purpose MBS algorithms must provide the option of efficiently solving numerically stiff systems without solely relying on low-order methods that have artificial numerical damping.

The TLISMNI method avoids numerical force differentiation, satisfies the nonlinear algebraic equations at the position, velocity, and acceleration levels, and exploits sparse matrix techniques [29]. The TLISMNI algorithm can be designed using several different integration methods such as the Hilber–Hughes–Taylor (HHT), trapezoidal, and BDF methods, the third- and fourth-order Adams integration methods, the higher-order symplectic implicit Runge–Kutta method, and the fourth-order BDF/EBDF method [1,15,17,30,44]. While second-order implicit methods have been successfully used in a large number of problems, low-order formulas do not allow performing an accurate MBS analysis in the case of high speed and highly nonlinear spinning motion. Moreover, the larger local truncation error resulting from lower-order formulas must be compensated for by taking smaller time steps in order to obtain the desired accuracy. The relatively higher-order TLISMNI/Adams method was proposed to address these concerns [30]. The performance of high-order implicit integration methods, such as the TLISMNI/Adams method, can be enhanced by designing error and time step selection criteria to minimize the number of outer loop iterations required to achieve convergence and to avoid unnecessary reductions in the time step.

6.2 Differential/algebraic equations

A constrained dynamical system is described by second-order differential equations of motion $\mathbf{M}\ddot{\mathbf{q}}+\mathbf{C}_{\mathbf{q}}^{T}\boldsymbol{\lambda}=\mathbf{Q}$ and by a set of algebraic constraint equations $\mathbf{C}(\mathbf{q},t)=\mathbf{0}$ which define mechanical joints and specified motion trajectories. In these motion and constraint equations, $\mathbf{M}$ is the system mass matrix, $\mathbf{q}$ is the system generalized coordinate vector, $\mathbf{C}$ is the constraint function vector, t is time, $\mathbf{C}_{\mathbf{q}}$ is the Jacobian matrix of the kinematic constraint equations, $\boldsymbol{\lambda}$ is the vector of Lagrange multipliers, and $\mathbf{Q}$ is the vector of generalized forces. The constraint equations at the velocity and acceleration levels can be obtained by taking the first and second time derivatives of the constraint equations $\mathbf{C}(\mathbf{q},t)=\mathbf{0}$ as $\mathbf{C}_{\mathbf{q}}\dot{\mathbf{q}}=-\mathbf{C}_{t}$ and $\mathbf{C}_{\mathbf{q}}\ddot{\mathbf{q}}=\mathbf{Q}_{c}$, respectively, where the subscript t represents the partial derivative with respect to time and $\mathbf{Q}_{c}$ is a vector that contains terms which are not linear in the accelerations. The equations of motion and the constraint equations at the acceleration level can be combined in one matrix equation as

$$\begin{bmatrix}\mathbf{M} & \mathbf{C}_{\mathbf{q}}^{T}\\ \mathbf{C}_{\mathbf{q}} & \mathbf{0}\end{bmatrix}\begin{bmatrix}\ddot{\mathbf{q}}\\ \boldsymbol{\lambda}\end{bmatrix}=\begin{bmatrix}\mathbf{Q}\\ \mathbf{Q}_{c}\end{bmatrix}. \tag{17}$$

The coefficient matrix in this equation is sparse, allowing for using sparse matrix techniques in order to efficiently solve for the accelerations and the vector of Lagrange multipliers.

6.3 TLISMNI/Adams method

The TLISMNI/Adams method, which is based on a constant order and a variable time step size, has two iterative loops: the *outer loop* and the *inner loop*. In the outer loop, the independent differential equations of motion are solved using the predictor Adams–Bashforth and corrector Adams–Moulton formulae, while in the inner loop the dependent variables are determined from the system degrees of freedom by solving the system of algebraic constraint equations. The two sets of independent and dependent coordinates $\mathbf{q}_i$ and $\mathbf{q}_d$ are identified using the constraint Jacobian matrix $\mathbf{C}_\mathbf{q}$. In the TLISMNI inner loop, the dependent coordinates are determined using a Newton–Raphson algorithm by iteratively solving the following sparse system of algebraic equations:

$$\begin{bmatrix} \mathbf{C}_\mathbf{q}^j \\ \mathbf{I}_i \end{bmatrix} \Delta\mathbf{q}^j = \begin{bmatrix} -\mathbf{C}^j \\ \mathbf{0} \end{bmatrix} \tag{18}$$

where $\Delta\mathbf{q}^j$ is the vector of Newton differences at iteration j and $\mathbf{I}_i$ is a Boolean matrix used to ensure that the independent coordinates remain fixed. Once the coordinates are determined, the dependent velocities can be calculated by solving the linear sparse matrix equation

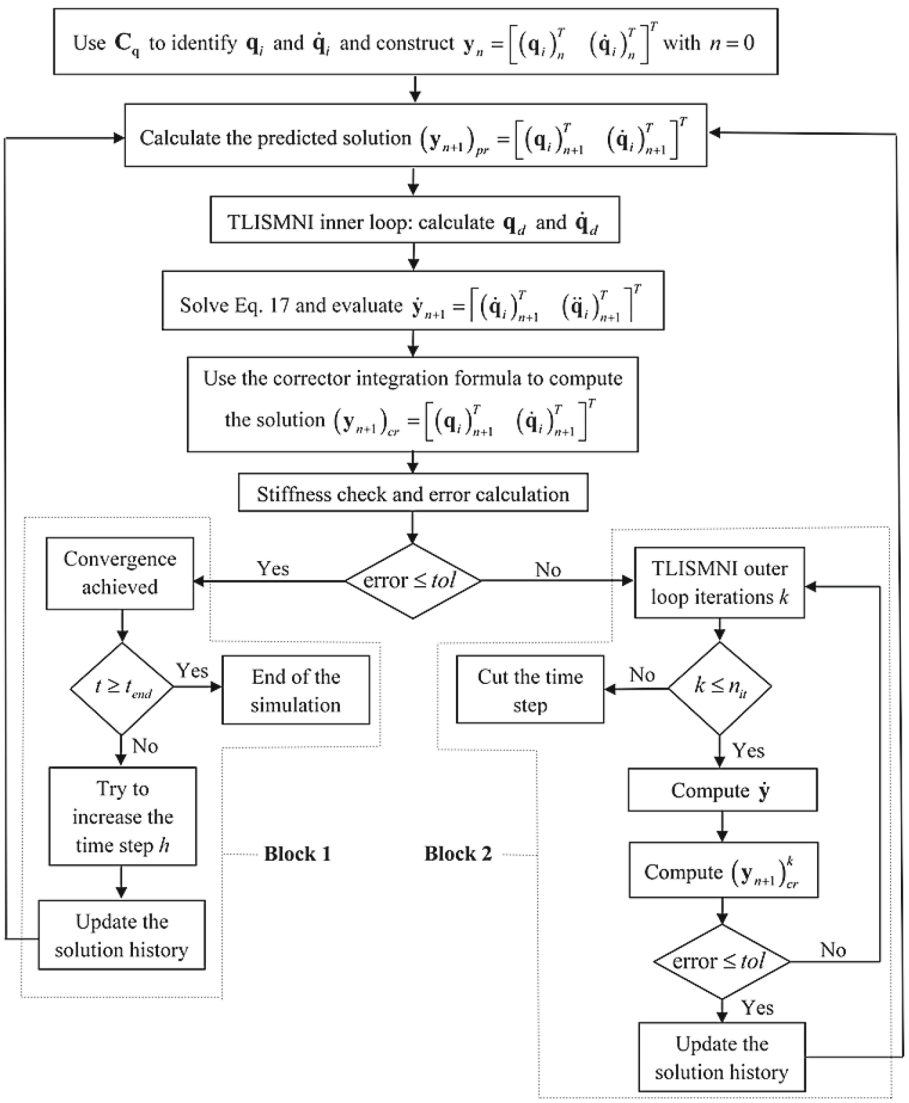

Fig. 7 TLISMNI flowchart

$$\begin{bmatrix} \mathbf{C}_{\mathbf{q}} \\ \mathbf{I}_i \end{bmatrix} \dot{\mathbf{q}} = \begin{bmatrix} -\mathbf{C}_t \\ \dot{\mathbf{q}}_i \end{bmatrix}. \tag{19}$$

After calculating the coordinates and velocities, Eq. (17) can be solved for the vectors of accelerations and Lagrange multipliers. The main steps of the TLISMNI/Adams algorithm are summarized in the flowchart shown in Fig. 7. The maximum number of outer loop iterations n_{it} is set to 5. The time step selection criterion adopted in this investigation is the same as the one presented previously in the literature [30]. The error check and stiffness detection scheme used in this investigation are discussed in the following Section.

7 Stiffness detection and error control

In the TLISMNI procedure, the equations of motion are converted to the state space form as $\dot{\mathbf{y}} = \mathbf{f}(\mathbf{y}, t)$, where $\mathbf{y} = \left[\mathbf{q}^T \ \dot{\mathbf{q}}^T\right]^T$, t is time, and $\mathbf{q}$ and $\dot{\mathbf{q}}$ are the vectors of system generalized coordinates and velocities, respectively. A differential equation of the form $\dot{\mathbf{y}} = \mathbf{f}(\mathbf{y}, t)$ can be defined as stiff if its Jacobian matrix $\mathbf{f}_{\mathbf{y}}(\mathbf{y}, t)$ is characterized by widely separated eigenvalues. Moreover, the solution of a stiff system is defined by components which exhibit very rapid changes. Explicit variable-order methods, such as the predictor–corrector Adams method, fail or become very inefficient in the case of stiff problems because the stability requirement reduces the order and the step size [31]. The reduction in the order of the integration formulas when stiffness is encountered is justified because past history details become less significant and the region of absolute stability of a method becomes larger as the order is decreased [3]. Implicit schemes, such as the low-order A-stable trapezoidal and BDF methods, are often used for the solution of stiff systems. However, there are no A-stable multistep methods with order higher than two, as shown by Dahlquist [8]. Higher-order implicit methods are, therefore, necessary to accurately capture rapid changes in the solution of stiff MBS applications characterized by high speed and highly nonlinear spinning motion. For this reason, it is important to design a stiffness (high-frequency) detection procedure which can be used with higher-order implicit integration methods, such as the TLISMNI/Adams algorithm, to obtain an efficient solution of stiff problems without compromising numerical accuracy.

The approach presented in this Section is based on the observation that repeated jumps in low-order derivatives arise from discontinuities, which lead to stiff systems. For this reason, the change in the low-order derivatives at successive time steps during the integration process can be used to shed light on the high-frequency contents in the solution. It is important, however, to point out that the analysis of jumps in low-order derivatives must be performed with care because jumps can also result from the accumulation of discretization errors due to the numerical approximations and from errors due to the use of a limited precision arithmetic. A flowchart of the proposed stiffness detection algorithm and error check is shown in Fig. 8. Using an approach similar to that proposed in the literature [17], the error at time step $n+1$ is computed as $|\boldsymbol{e}_{n+1}| = \sqrt{\sum_{i=1}^{N} \left[(\Delta y)_i/(Y)_i\right]^2}$, where N is the number of independent coordinates, $\Delta\mathbf{y}$ is defined as the difference between the components of the corrector and predictor vectors $\mathbf{y}_{cr}$ and $\mathbf{y}_{pr}$ as $(\Delta y)_i = (y_{cr})_i - (y_{pr})_i$, and $\mathbf{Y}$ is a weighted vector such that $(Y)_i = \max\left[1, \ (y_{cr})_i\right]$. The process of identifying high frequencies or rapid changes starts with the calculation, at each time step, of the two vectors $\mathbf{s}_1$ and $\mathbf{s}_2$, defined as

$$(\mathbf{s}_j)_k = (\dot{\mathbf{y}}_n - \dot{\mathbf{y}}_{n-j})_k / (\dot{\mathbf{y}}_{n-j})_k \quad j = 1, 2, \tag{20}$$

where $\dot{\mathbf{y}}_n$, $\dot{\mathbf{y}}_{n-1}$ and $\dot{\mathbf{y}}_{n-2}$ contain information on the low-order derivatives at time steps n, $n-1$, and $n-2$, and k is the element number. The vectors $\mathbf{s}_1$ and $\mathbf{s}_2$ measure the relative change in each component of the state vector $\dot{\mathbf{y}}$ at the three time steps prior to step $n+1$. The use of a relative measure is preferred over an absolute measure because it allows for performing an analysis which is not coordinate-dependent. It is important to notice that using more than two vectors $\mathbf{s}_j$ can lead to a significant increase in the storage memory required, especially in the case of large systems of equations. The next step consists of checking each component of $\mathbf{s}_1$ and $\mathbf{s}_2$ against a parameter η which serves as an indicator of stiffness. The value of η must be carefully defined based on extensive numerical experimentation. If the absolute value of an element of the vectors of Eq. (20) is larger than η, the corresponding coordinate is assumed to have a high frequency. In the numerical implementation, the frequency check is made using the vector $\mathbf{w}$, whose components are defined as

$$w_i = \max\left[\left|(s_1)_i\right|, \left|(s_2)_i\right|\right], \quad i = 1, \ldots, N. \tag{21}$$

If at least one component of $\mathbf{w}$ is larger than η, a stiffness counter is increased one unit. The stiffness test consists of a sequence of 50 consecutive steps in which the value of the stiffness counter is increased. The

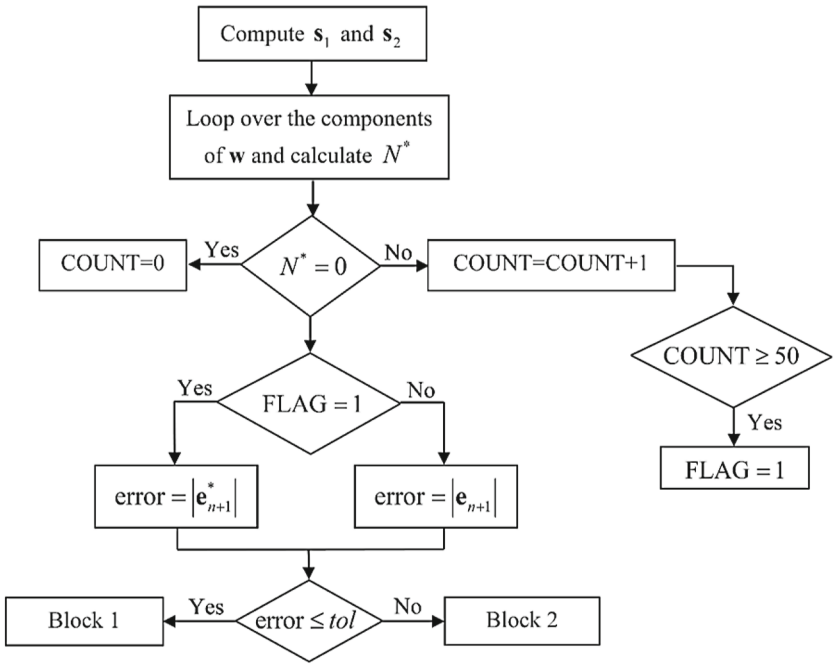

Fig. 8 Flowchart of the stiffness detection algorithm and error estimation.

number of consecutive steps is selected using a procedure consistent with the stiffness indicator implemented in the code DE by Shampine and Gordon [31]. Once a stiff behavior is identified, a flag variable is set equal to 1 and the error formula is modified to

$$\left|\boldsymbol{e}^*_{n+1}\right| = \sqrt{\sum_{i=1}^{N^*} \left[(\Delta y)_i/(Y)_i\right]^2}, \quad i = 1, \ldots, N^* \tag{22}$$

where N^* is the number of non-stiff components of the vector $\mathbf{w}$. The solution at time step $n+1$ is accepted if the error is less than the user specified tolerance *tol*. Neglecting the contribution of selected stiff independent coordinates in the calculation of the error allows avoiding reductions in the time step, minimizes the number of outer loop iterations, and significantly reduces unnecessary calculations which can negatively impact the computational efficiency.

8 Numerical results

In this Section, several numerical examples which include ANCF high-frequency oscillations are studied in order to demonstrate the effectiveness and efficiency of the proposed Navier–Stokes viscoelastic constitutive model and the new TLISMNI error control criterion. The first three numerical examples are used to examine the effect of the proposed viscous damping formulation in small and large deformation problems. In the first example, the small deformation of a stiff cantilever beam is investigated, and the final equilibrium position of the tip node is verified against the reference solution obtained using the commercial FE software ANSYS®. In the second example, the large deformation of a flexible pendulum with moving base is studied. In the third example, the ANCF high-frequency tire oscillations produced during pressurization are analyzed. It is found that accounting for the viscoelasticity allows for damping out high-frequency oscillations and leads to a 50–65% reduction in CPU simulation time as compared to the undamped case.

The last two examples are used to demonstrate the use of TLISMNI/Adams algorithm for solving stiff problems characterized by ANCF high-frequency oscillations. The results obtained for the implicit third-order TLISMNI/Adams algorithm, the explicit Adams predictor–corrector method, and the TLISMNI/HHT method are compared in terms of accuracy, efficiency, and damping characteristics. The stiffness parameter used in the TLISMNI/Adams algorithm is $\eta = 10$, while the TLISMNI/HHT method is used with the maximum allowed numerical damping $\alpha = -0.3$ [17]. The simulations were performed on a PC with an Intel i5 3.40GHz

processor and 8 GB RAM. In all the examples, the elastic forces are formulated using the general continuum mechanics approach.

8.1 Cantilever beam

In the first example, a cantilever beam subjected to a vertical concentrated load at its free end is analyzed. The beam is assumed to have a length of 1 m and a square cross section with dimension 0.1 m, as shown in Fig. 9. Young's modulus and material density are assumed 2×10^{11} Pa and 7800 kg/m^3, respectively. The dynamic viscosity coefficient μ is assumed 10^6 Pa $\cdot$ s, based on the analysis of Sect. 3. The cantilever beam is meshed using 10 three-dimensional fully parameterized ANCF beam elements, which allow correctly describing finite rigid body rotation, lead to zero strain under arbitrary rigid body displacement, and account for both shear deformation and rotary inertia. In order to alleviate the Poisson locking, Poisson's ratio ν is assumed zero, an assumption often made in the literature when using benchmark examples ([13,34,45]). The effect of the gravitational force is also neglected. The equilibrium position of the beam free end is compared with the reference solution obtained using ANSYS® BEAM188 elements. The external load is assumed initially zero and reaches the steady-state value F at time t_0 according to

$$\left.\begin{array}{ll} (F/2)\left[1-\cos\left(\pi t/t_0\right)\right] & \text{if } t \le t_0 \\ F & \text{if } t > t_0 \end{array}\right\}. \tag{23}$$

The value of F is selected 50 kN so that the cantilever beam can experience small oscillations. First, a quasi-static analysis is performed by gradually applying the load ($t_0 = 4$ s) during the first 5 s of simulation time, and

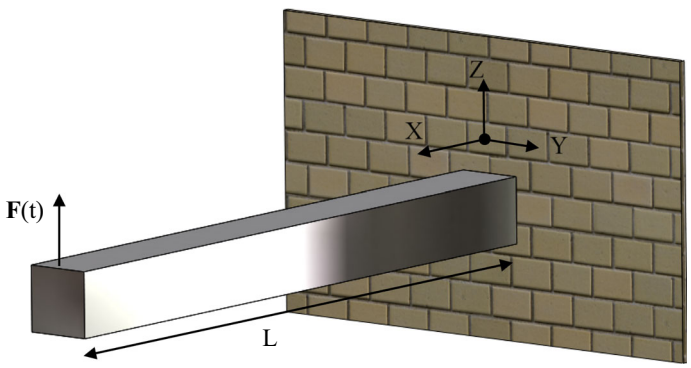

Fig. 9 Cantilever beam subjected to tip vertical load

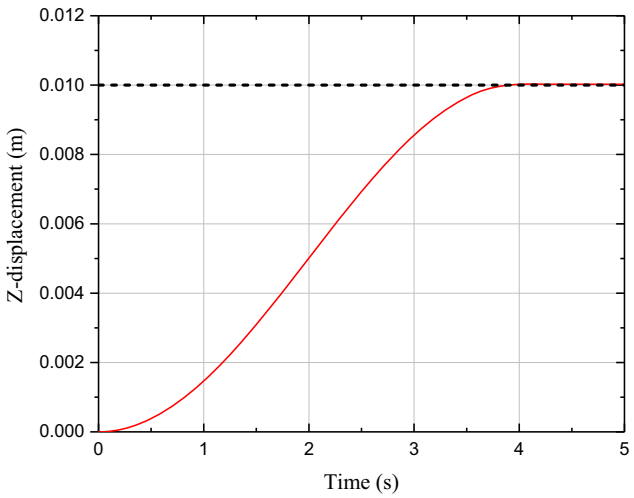

Fig. 10 Vertical displacement of the beam tip. Quasi-static analysis (——— ANCF, - - - - static)

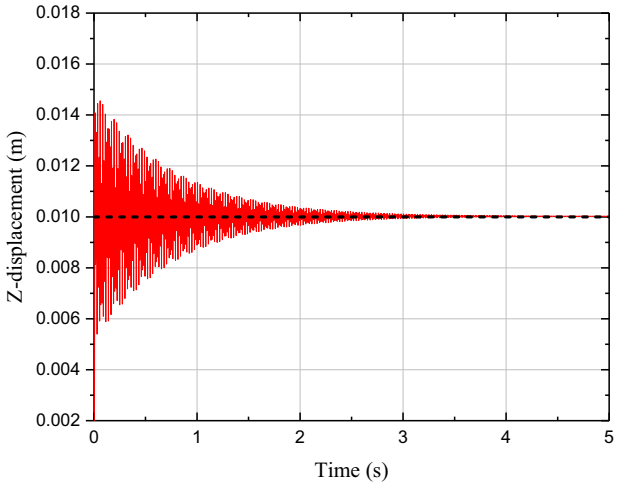

Fig. 11 Vertical displacement of the beam tip. Dynamic analysis (——— ANCF, - - - - static)

the results are shown in Fig. 10. In order to test the ability of the viscoelastic constitutive model to damp out high-frequency oscillations, the value of t_0 is reduced to 0.01 s. The solution in this case is shown in Fig. 11. It is clear that the steady-state results of the quasi-static and dynamic analyses coincide with the static solution (0.010 m). The results shown in this example demonstrate that the proposed viscoelastic constitutive model is effective in damping out ANCF high-frequency oscillations.

8.2 Pendulum with moving base

In this example, the oscillation of a pendulum subjected to a uniform distributed gravity force is studied to examine the effect of the viscoelastic constitutive model in the analysis of very flexible and incompressible rubberlike materials. The initial configuration of the system is shown in Fig. 12, and the problem data are provided in Table 1. The base of the pendulum is subjected to a prescribed harmonic motion defined by $X = X_0 \sin \omega t$, where $X_0 = -0.02$ m and $\omega = 2\pi$ rad/s. The pendulum is meshed using 4 three-dimensional fully parameterized ANCF beam elements. This problem was previously analyzed in the literature [20] to test the implementation of ANCF elastic force formulations, such as the neo-Hookean and Mooney–Rivlin, for rubber materials. The vertical position of the pendulum tip is shown in Fig. 13 for the damped and undamped scenarios. The results obtained show that there is no significant difference between the vertical tip displacements using different models. Nonetheless, a reduction of nearly 50% of the CPU time is achieved when the viscoelastic constitutive model is used. Figure 14 shows the determinant J of the matrix of position vector gradients $\mathbf{J}$ at the tip of the pendulum as a function of time when using the incompressible neo-Hookean constitutive law. It is clear that the use of the viscoelastic formulation allows damping out the high-frequency oscillations of J. The position vector gradients of the beam cross section $\mathbf{r}_y$ and $\mathbf{r}_z$, which are important indicators of the cross-sectional deformation, can exhibit high-frequency oscillations that do not have a significant effect on the

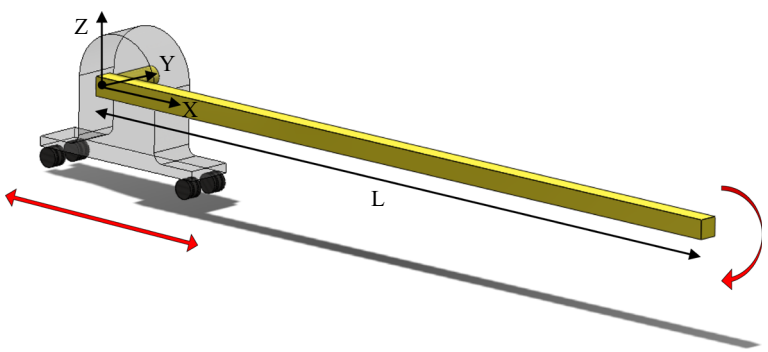

Fig. 12 Flexible pendulum with moving base

Table 1 Material and geometric properties of the pendulum with moving base

Property	Quantity
Length L (m)	1.0
Cross-sectional area (m^2)	0.02×0.02
Density ρ (kg/m^3)	7200
Poisson's ratio ν	0.3
Young's modulus E (Pa)	2×10^6
Mooney–Rivlin coefficient μ_{10} (Pa)	0.8×10^6
Mooney–Rivlin coefficient μ_{01} (Pa)	0.2×10^6
Incompressibility constant k (Pa)	10^9
Dynamic viscosity μ (Pa · s)	10

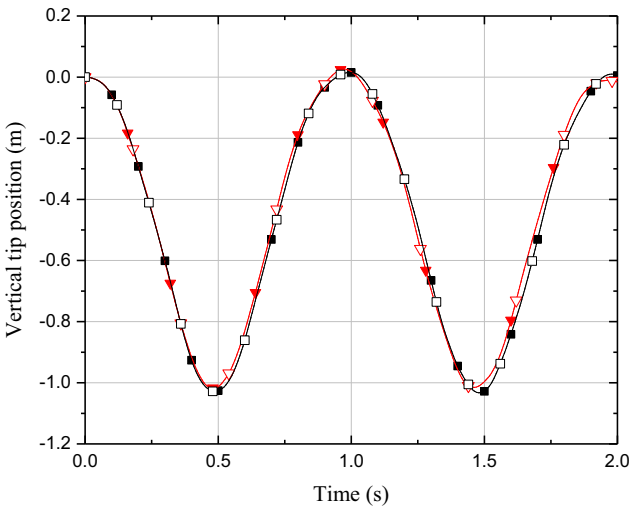

Fig. 13 Vertical position of the pendulum tip (neo-Hookean: —□— damped, ----■---- undamped; Mooney–Rivlin: —▽— damped, ----▼---- undamped)

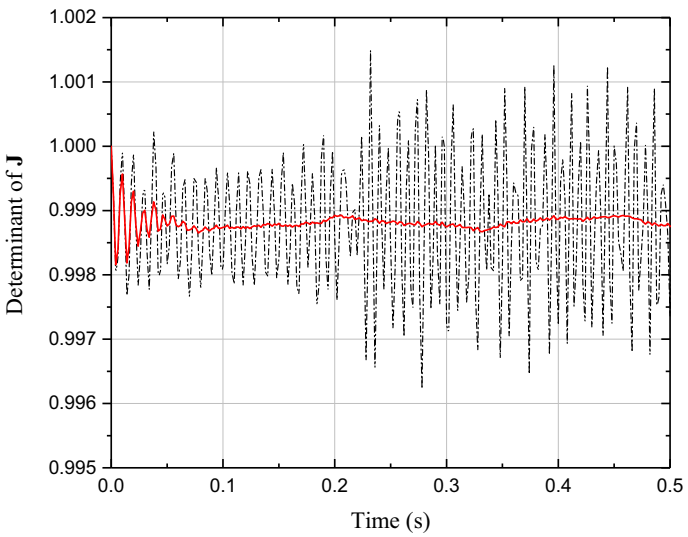

Fig. 14 Determinant of the matrix of position vector gradients (damped, undamped)

solution in this problem, but lead to a significant increase in the CPU time. Figure 15 shows the variation of the norm of $\mathbf{r}_y$ at the tip of the pendulum as a function of time in the undamped and damped cases when the elastic Mooney–Rivlin constitutive law is used. As expected, the use of the viscoelastic constitutive model results in damping out the high-frequency oscillations of the position vector gradients of the beam cross section.

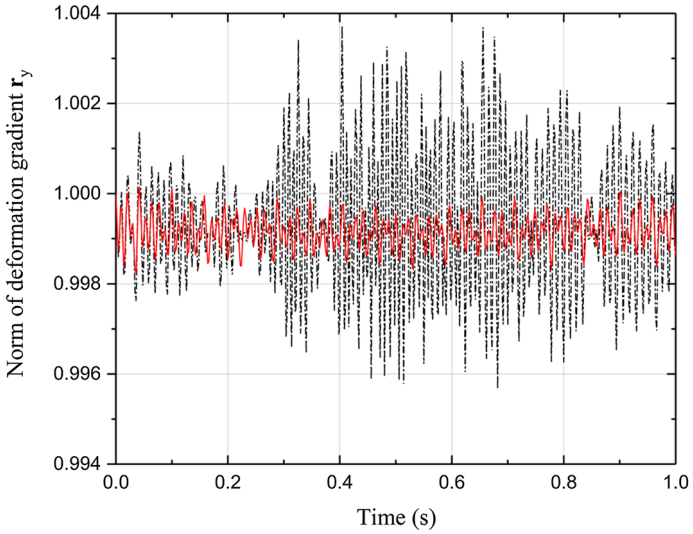

Fig. 15 Norm of gradient $\mathbf{r}_y$ at the pendulum tip (damped, undamped)

8.3 Tire pressurization

In this example, the ANCF high-frequency oscillations exhibited by a pneumatic tire during pressurization are analyzed. The tire geometry, shown in Fig. 16, is based on the 11R22.5 model manufactured by Michelin [21]. The material has density 1500 kg/m^3, modulus of rigidity 10^8 N/m^2, Young's modulus 2×10^8 N/m^2, and dynamic viscosity 1000 Pa $\cdot$ s. The tire FE model is meshed using 24 fully parameterized ANCF plate elements, and the rigid rim is modeled using an ANCF *reference node* [24,28]. The effects of localized geometries on the tire tread such as grooves are not included in this model. The vector of generalized continuum-based air pressure forces applied to the internal surface of ANCF element j can be written as $\mathbf{Q}_p^j = \int_{S_0^j} \left(\mathbf{S}^j\right)^T \left(J^j p_t \mathbf{n}^j / \sqrt{\left(\mathbf{n}^j\right)^T \mathbf{J}^j \left(\mathbf{J}^j\right)^T \mathbf{n}^j} \right) dS_0^j$, where $\mathbf{S}^j$ is the shape function matrix, S_0^j is the element area in the reference configuration, $\mathbf{n}^j$ is the unit normal to the surface, p_t is the pressure magnitude, and J^j is the determinant of the matrix of position vector gradients $\mathbf{J}^j$ [24,28]. The pressure magnitude is assumed $p_t = 90$ psi, while the effect of gravity is neglected. Figure 17 shows a comparison between the radial deformation of node 1 during pressurization in the damped and undamped cases. Clearly, the viscoelastic constitutive model allows damping out the vibrations of the tire and reaching a steady-state equilibrium configuration. Moreover, the use of the viscoelastic constitutive model leads to a 65% reduction in the CPU time compared to the purely elastic case.

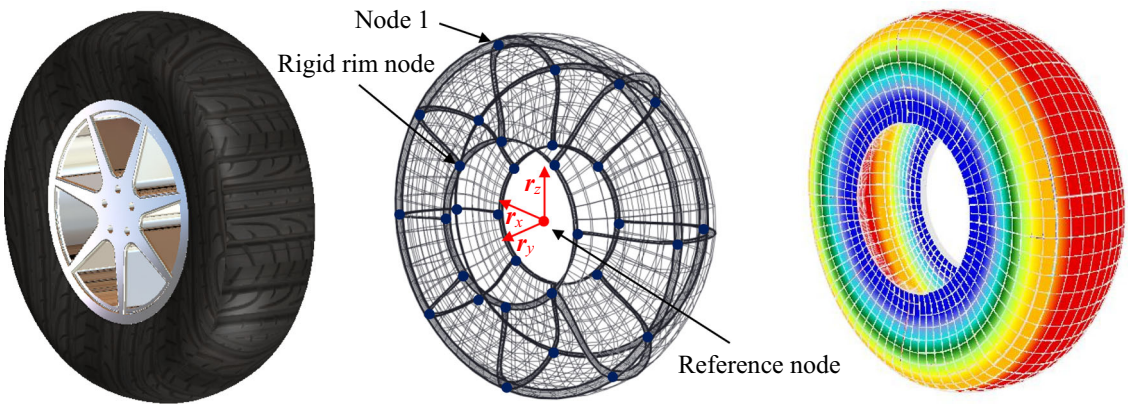

Fig. 16 From left to right: CAD, ANCF element, and pressurized tire model

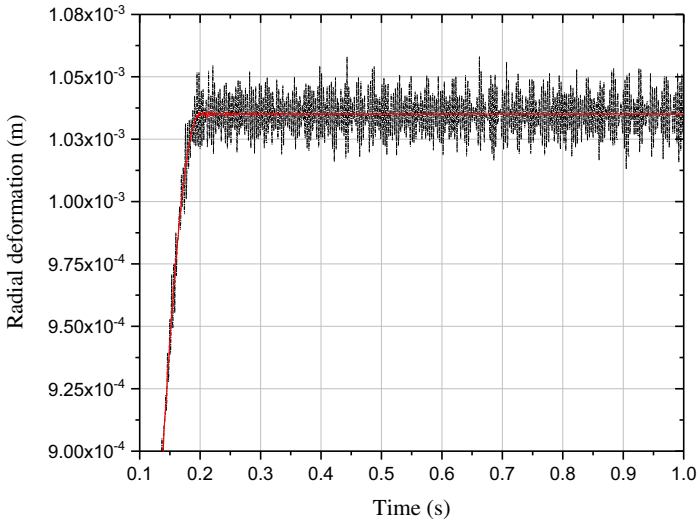

Fig. 17 Radial deformation of node 1 of the ANCF tire model (damped, undamped)

8.4 Planar pendulum

In this example, an initially horizontal planar pendulum falling under the effect of gravity is considered, as shown in Fig. 18. This problem is similar to the example previously used in the literature [17]. The pendulum is connected to the ground by a revolute joint and is modeled using eight two-dimensional shear-deformable ANCF beam elements. The pendulum has an initial length of 0.4 m, square cross-sectional area of 0.04×0.04 m^2, density 7800 kg/m^3, Young's modulus 2×10^{11} N/m^2, and Poisson's ratio 0.3. The gravitational acceleration constant g is assumed to be 9.81 m/s^2. For this stiff problem, the transverse deformation of the beam is dominated by the frequency of the free-falling motion, which has a periodic time of nearly 1.2 s, and by the beam's first and second bending modes. The beam midpoint transverse and axial deformations are measured as shown in Fig. 19. Figures 20 and 21 show a comparison between the midpoint transverse deformations obtained using different integration methods. It is clear that the TLISMNI/Adams algorithm and the explicit Adams method agree well in capturing the high-frequency content of the solution. On the

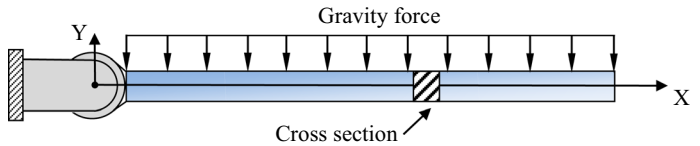

Fig. 18 Initial configuration of the planar pendulum

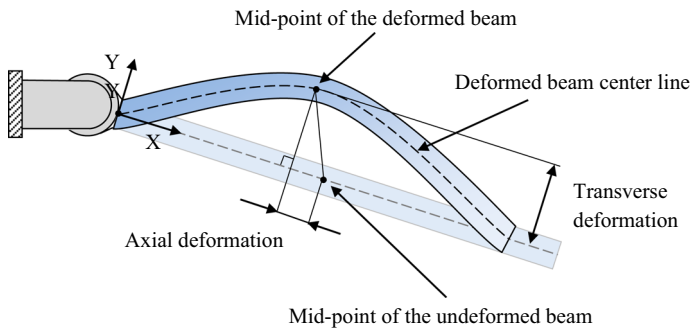

Fig. 19 Midpoint transverse and axial deformations

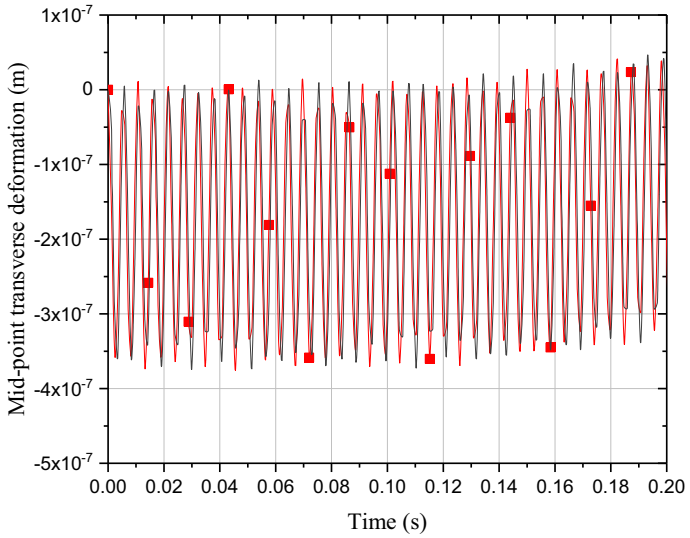

Fig. 20 Pendulum midpoint transverse deformation for a short time interval (Explicit Adams; TLISMNI/Adams)

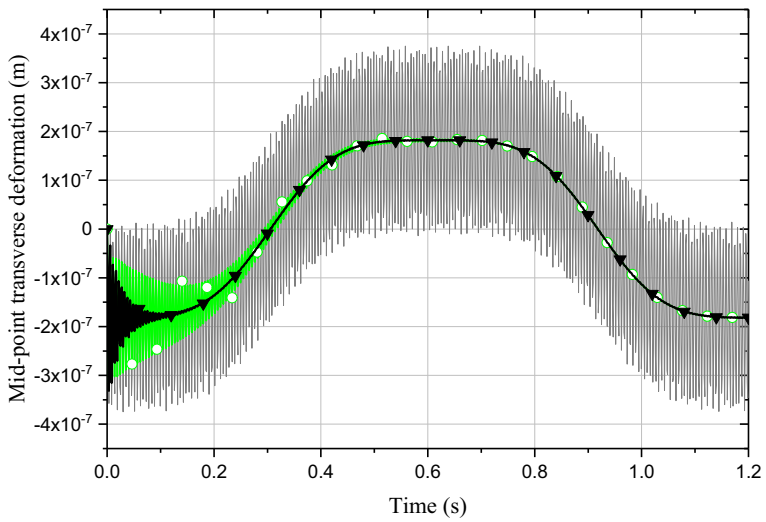

Fig. 21 Pendulum midpoint transverse deformation (TLISMNI/HHT; TLISMNI/Adams; TLISMNI/Adams–damped $\mu = 2 \cdot 10^5$ Pa · s)

other hand, the TLISMNI/HHT method produces a smoother solution by filtering out the first and second bending modes. It is observed that if the TLISMNI/Adams algorithm is used with the newly proposed Navier–Stokes physical damping, the two fundamental bending modes are damped out at a faster rate compared to the TLISMNI/HHT method. In Fig. 22, the CPU time required to simulate the same example using different values of Young's modulus is shown; these values are 2×10^6, 2×10^7, 2×10^8, 2×10^9, 2×10^{10}, 2×10^{11} N/m^2. It can be noticed that as the stiffness of the system increases, the TLISMNI/Adams method becomes nearly four times faster than the explicit Adams method. The TLISMNI/Adams and TLISMNI/HHT methods have a similar degree of computational efficiency for the entire range of Young's modulus. Furthermore, the TLISMNI/Adams CPU time obtained when physical damping is used is less than the CPU time in the case of zero damping.

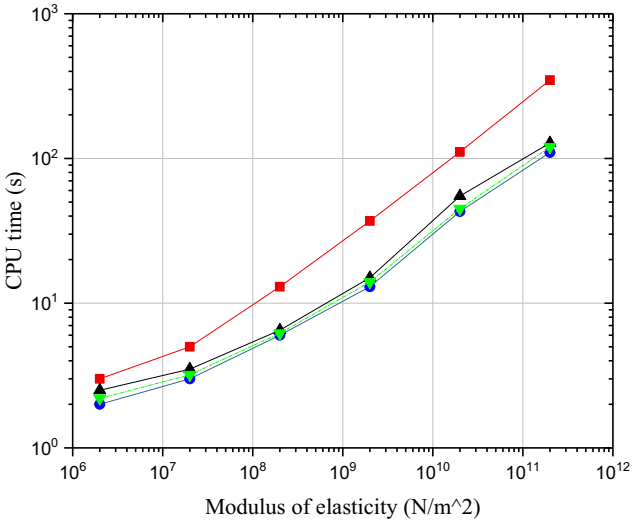

Fig. 22 CPU time versus modulus of elasticity for the pendulum problem (Explicit Adams; TLISMNI/Adams; TLISMNI/Adams–damped; TLISMNI/HHT)

8.5 Planar slider crank mechanism

The planar slider crank mechanism considered in this example, and shown in Fig. 23, is the same as the one used in the literature [10,22]. The crankshaft is assumed to have a constant angular velocity $\omega = \pi$ rad/s and a mass moment of inertia with respect to its the mass center 0.015 kg $\cdot$ m^2. The connecting rod, which is horizontal in

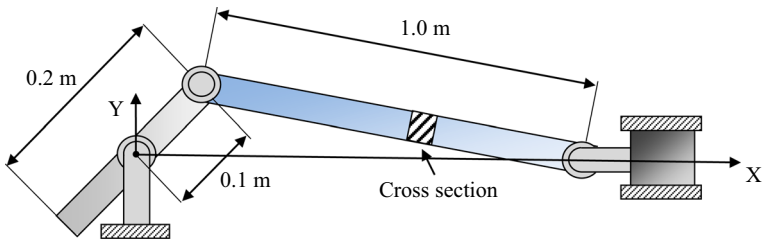

Fig. 23 Slider crank mechanism

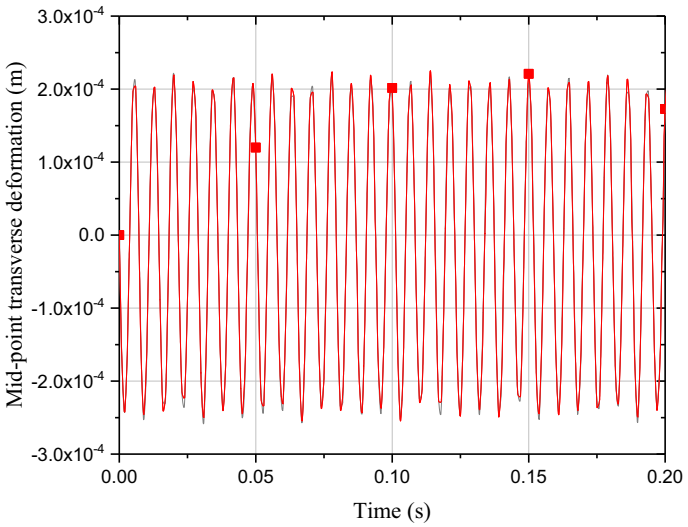

Fig. 24 Connecting-rod midpoint transverse deformation for a short time interval (Explicit Adams; TLISMNI/Adams)

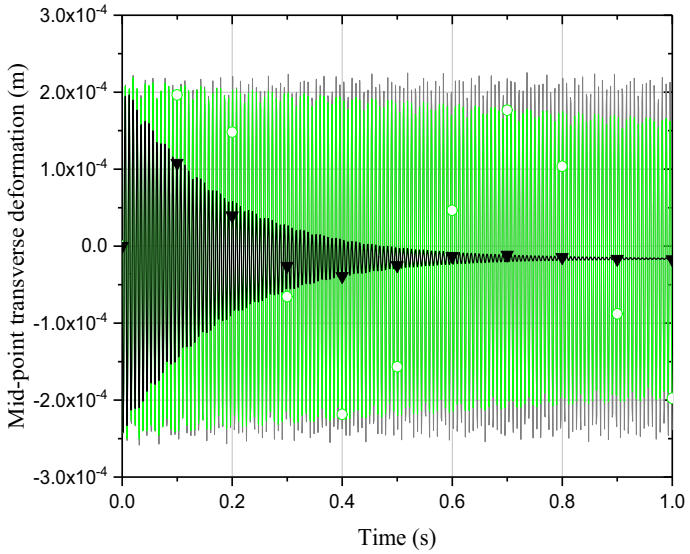

Fig. 25 Connecting-rod midpoint transverse deformation (TLISMNI/Adams; TLISMNI/HHT; TLISMNI/Adams–damped $\mu = 2 \cdot 10^6$ Pa · s)

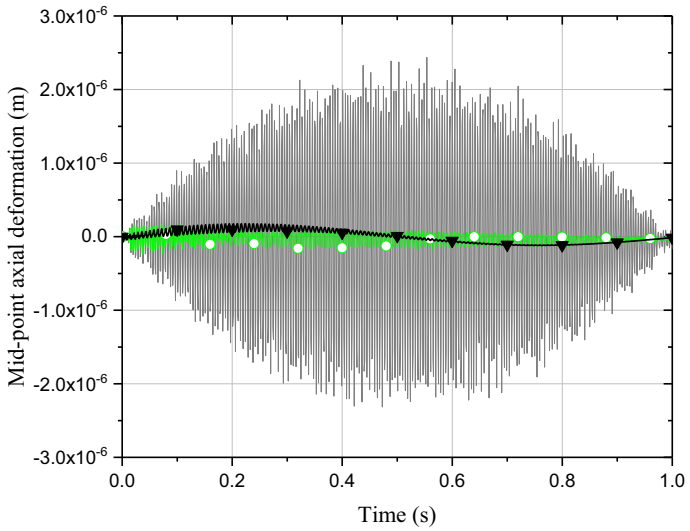

Fig. 26 Connecting-rod midpoint axial deformation (TLISMNI/Adams; TLISMNI/HHT; TLISMNI/Adams–damped $\mu = 2 \cdot 10^6$ Pa · s)

the initial configuration, has an undeformed length of 1.0 m and a square cross-sectional area 0.05×0.05 m^2. The connecting rod is modeled using eight two-dimensional shear-deformable ANCF beam elements that have a density 7200 kg/m^3, Young's modulus 2×10^8 N/m^2, and Poisson's ratio 0.3. The slider block has a mass 1.0 kg. The midpoint transverse and axial deformations of the connecting rod, which are measured as shown in Fig. 19, are used to compare the results obtained using different numerical integration methods. As was the case with the planar pendulum example, Fig. 24 shows that the TLISMNI/Adams algorithm and the explicit Adams method agree well in capturing the high-frequency content of the midpoint transverse deformation. With regard to the damping effectiveness of each method, it can be noted that the TLISMNI/HHT method successfully damps out the axial mode but is less efficient than the physically damped TLISMNI/Adams algorithm in filtering out the transverse bending mode, as shown in Figs. 25 and 26. In order to compare the computational efficiency of each method, the CPU time required to simulate the same example using different values of the elasticity coefficient is shown in Fig. 27. It is clear that while there is a good agreement between

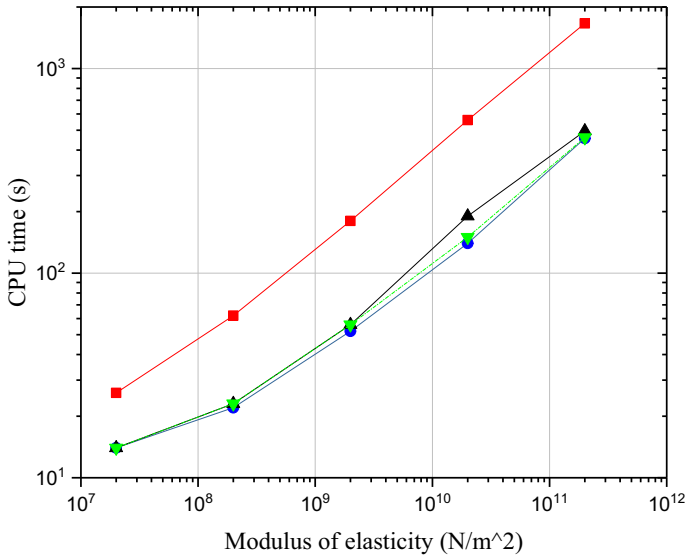

Fig. 27 CPU time versus modulus of elasticity for the slider crank problem (Explicit Adams; TLISMNI/Adams; TLISMNI/Adams–damped; TLISMNI/HHT)

the TLISMNI/HHT and TLISMNI/Adams methods in terms of computational efficiency, in the case of a stiff system the explicit Adams method becomes four times slower than the TLISMNI implicit methods.

9 Summary and conclusions

High-frequency ANCF coupled deformation modes can be the source of numerical problems if appropriate solution techniques are not used. In this paper, two techniques are proposed to eliminate or damp out ANCF high-frequency modes and efficiently solve stiff systems of differential/algebraic equations. A new objective viscoelastic constitutive model which can be used in the study of small and large deformations of incompressible and very flexible materials is proposed. The elastic forces are formulated using general hyperelastic strain energy density functions, and the viscous damping forces are defined using the Navier–Stokes equations, widely used for fluids. This paper extends the use of the Navier–Stokes equations for solids modeled using ANCF elements. The novelty of the proposed viscoelastic constitutive model in comparison with existing formulations, such as the small strain and ANCF DGRV models, is discussed. The Navier–Stokes viscoelastic approach for ANCF solids is validated using analytical and numerical results and is tested using several numerical examples. It is shown that the proposed viscoelastic formulation can efficiently damp out ANCF high-frequency modes and leads to a reduction in simulation time of at least 50% compared to the undamped case. A new error control criterion based on a stiffness detection algorithm is proposed for the variable step-size TLISMNI method to allow evaluating the significance of each solution coordinate during the integration process. This criterion is used to filter out insignificant high-frequency components. The TLISMNI method exploits sparse matrix techniques, satisfies the algebraic constraint equations at the position, velocity, and acceleration levels, and avoids numerical force differentiation, which can be a source of error when bodies with high stiffness are considered. The proposed error control criterion is tested with the third-order TLISMNI/Adams method by solving several numerical examples. The TLISMNI/Adams method is compared to the TLISMNI/HHT and the explicit predictor–corrector Adams methods in terms of efficiency, accuracy, and damping characteristics. It is shown that the TLISMNI/Adams method becomes nearly four times faster than the explicit Adams method in case of stiff systems. It is also noted that the TLISMNI/Adams method can achieve the same level of computational efficiency as the TLISMNI/HHT method, which is based on low-order integration formulas and makes use of artificial numerical damping. It is shown that the Navier–Stokes viscoelastic constitutive model used with the TLISMNI/Adams method can damp out ANCF high-frequency oscillations at a faster rate compared to the TLISMNI/HHT method.

Acknowledgements This research was supported by the National Science Foundation (Project # 1632302).

References

1. Aboubakr, A., Shabana, A.A.: Efficient and robust implementation of the TLISMNI method. J. Sound Vib. **353**, 220–242 (2015)
2. Araki, T., White, J.L.: Shear viscosity of rubber modified thermoplastics: dynamically vulcanized thermoplastic elastomers and ABS resins at very low stress. Polym. Eng. Sci. **38**(4), 590–595 (1998)
3. Atkinson, K.E.: An Introduction to Numerical Analysis. Wiley, New York (1978)
4. Bathe, K.J.: Finite Element Procedures. Prentice Hall, New Jersey (1996)
5. Belytschko, T., Liu, W.K., Moran, B., Elkhodary, K.: Nonlinear Finite Elements for Continua and Structures. Wiley, Chichester (2013)
6. Casalini, R., Bogoslovov, R., Qadri, S.B., Roland, C.M.: Nanofiller reinforcement of elastomeric polyurea. Polymer **53**(6), 1282–1287 (2012)
7. Chapman, B., Jost, G., Van Der Pas, R.: Using OpenMP: Portable Shared Memory Parallel Programming. MIT press, Cambridge (2008)
8. Dahlquist, G.G.: A special stability problem for linear multistep methods. BIT Numer. Math. **3**(1), 27–43 (1963)
9. Deribas, A.A.: Physics of Hardening and Explosive Welding. Nauka, SO (1980)
10. Dmitrochenko, O.N., Hussein, B.A., Shabana, A.A.: Coupled deformation modes in the large deformation finite element analysis: generalization. J. Comput. Nonlinear Dyn. **4**(2), 021002-1–021002-8 (2009)
11. Drapaca, C.S., Sivaloganathan, S., Tenti, G.: Nonlinear constitutive laws in viscoelasticity. Math. Mech. Solids **12**(5), 475–501 (2007)
12. Fung, Y.-C.: A First Course in Continuum Mechanics. Prentice-Hall, New Jersey (1977)
13. Garcia, D., Valverde, J., Dominguez, J.: An internal damping model for the absolute nodal coordinate formulation. Nonlinear Dyn. **42**(4), 347–369 (2005)
14. Gerstmayr, J., Sugiyama, H., Mikkola, A.: Review on the absolute nodal coordinate formulation for large deformation analysis of multibody systems. J. Comput. Nonlinear Dyn. **8**(3), 031016 (2013)
15. Guo, X., Zhang, D.G., Li, L., Zhang, L.: Application of the two-loop procedure in multibody dynamics with contact and constraint. J. Sound Vib. **427**, 15–27 (2018)
16. Hilber, H.M., Hughes, T.J., Taylor, R.L.: Improved numerical dissipation for time integration algorithms in structural dynamics. Earthq. Eng. Struct. Dyn. **5**(3), 283–292 (1977)
17. Hussein, B.A., Shabana, A.A.: Sparse matrix implicit numerical integration of the stiff differential/algebraic equations: implementation. Nonlinear Dyn. **65**(4), 369–382 (2011)
18. Kobayashi, H., Hiki, Y., Takahashi, H.: An experimental study on the shear viscosity of solids. J. Appl. Phys. **80**(1), 122–130 (1996)
19. Kobayashi, H., Takahashi, H., Hiki, Y.: A new apparatus for measuring high viscosity of solids. Int. J. Thermophys. **16**(2), 577–584 (1995)
20. Maqueda, L.G., Shabana, A.A.: Poisson modes and general nonlinear constitutive models in the large displacement analysis of beams. Multibody Syst. Dyn. **18**(3), 375–396 (2007)
21. Michelin, *Michelin Truck Tire Data Book*, 2016, 18th edition, p. 18
22. Mohamed, A.N.A., Shabana, A.A.: A nonlinear visco-elastic constitutive model for large rotation finite element formulations. Multibody Syst. Dyn. **26**(1), 57–79 (2011)
23. Nashif, A.D., Jones, D.I., Henderson, J.P.: Vibration Damping. Wiley, New York (1985)
24. Patel, M., Orzechowski, G., Tian, Q., Shabana, A.A.: A new multibody system approach for tire modeling using ANCF finite elements. Proc. Inst. Mech. Eng. K J. Multibody Dyn. **230**(1), 69–84 (2016)
25. Savenkov, G.G., Meshcheryakov, Y.I.: Structural viscosity of solids. Combust. Explos. Shock Waves **38**(3), 352–357 (2002)
26. Schmidt, A., Gaul, L.: Finite element formulation of viscoelastic constitutive equations using fractional time derivatives. Nonlinear Dyn. **29**(1–4), 37–55 (2002)
27. Serikov, S.V.: Estimate of the ultimate deformation in the rupture of metal pipes subjected to intense loads. J. Appl. Mech. Tech. Phys. **28**(1), 149–156 (1987)
28. Shabana, A.A.: Computational Continuum Mechanics, 3rd edn. Wiley, Chichester (2018)
29. Shabana, A.A., Hussein, B.A.: A two-loop sparse matrix numerical integration procedure for the solution of differential/algebraic equations: application to multibody systems. J. Sound Vib. **327**, 557–563 (2009)
30. Shabana, A.A., Zhang, D., Wang, G.: TLISMNI/Adams algorithm for the solution of the differential/algebraic equations of constrained dynamical systems. Proc. Inst. Mech. Eng. K J. Multibody Dyn. **232**(1), 129–149 (2018)
31. Shampine, L.F., Gordon, M.K.: Computer Solution of Ordinary Differential Equations: The Initial Value Problem. Freeman, San Francisco (1975)
32. Simo, J.C., Hughes, T.J.: Computational Inelasticity. Springer, Berlin (2006)
33. Snowdon, J.C.: Vibration and Shock in Damped Mechanical Systems. Wiley, New York (1968)
34. Sopanen, J.T., Mikkola, A.M.: Description of elastic forces in absolute nodal coordinate formulation. Nonlinear Dyn. **34**(1–2), 53–74 (2003)
35. Spencer, A.J.M.: Continuum Mechanics. Longman, London (1980)
36. Stepanov, G.V.: Elastoplastic Deformation of Materials under Pulse Loads. Naukova Dumka, Kiev (1979)
37. Stepanov, G.V.: Effect of strain rate on the characteristics of elastoplastic deformation of metallic materials. J. Appl. Mech. Tech. Phys. **23**(1), 141–146 (1982)
38. Takahashi, Y., Shimizu, N., Suzuki, K.: Introduction of damping matrix into absolute nodal coordinate formulation. In: The Proceedings of the Asian Conference on Multibody Dynamics 33–40 (2002)
39. Ugural, A.C., Fenster, S.K.: Advanced Strength and Applied Elasticity, 3rd edn. Prentice-Hall, New Jersey (1995)
40. White, F.M.: Fluid Mechanics, 5th edn. McGraw Hill, New York (2003)

41. White, J.L., Han, M.H., Nakajima, N., Brzoskowski, R.: The influence of materials of construction on biconical rotor and capillary measurements of shear viscosity of rubber and its compounds and considerations of slippage. J. Rheol. **35**(1), 167–189 (1991)
42. Wineman, A.: Nonlinear viscoelastic solids—a review. Math. Mech. Solids **14**(3), 300–366 (2009)
43. Yoo, W.S., Lee, J.H., Park, S.J., Sohn, J.H., Dmitrochenko, O., Pogorelov, D.: Large oscillations of a thin Cantilever beam: physical experiments and simulation using the absolute nodal coordinate formulation. Nonlinear Dyn. **34**(1–2), 3–29 (2003)
44. Zhang, L., Zhang, D.: A two-loop procedure based on implicit Runge–Kutta method for index-3 Dae of constrained dynamic problems. Nonlinear Dyn. **85**(1), 263–280 (2016)
45. Zhang, Y., Tian, Q., Chen, L., Yang, J.J.: Simulation of a viscoelastic flexible multibody system using absolute nodal coordinate and fractional derivative methods. Multibody Syst. Dyn. **21**(3), 281–303 (2009)